

Original Article

Analysis of Electron Transparent Beam-Sensitive Samples Using Scanning Electron Microscopy Coupled With Energy-Dispersive X-ray Spectroscopy

Anders Brostrøm^{1,2} , Kirsten Inga Kling^{1,3}, Karin Sørig Hougaard² and Kristian Mølhav^{1*}

¹Technical University of Denmark, DTU Nanolab – National Centre for Nano Fabrication and Characterization, Fysikvej, Building 307, Kgs Lyngby 2800, Denmark;

²National Research Centre for the Working Environment, Lersø Parkallé 105, Copenhagen 2100, Denmark and ³SAXOCON A/S, Bredevej 2D, Virum 2830, Denmark

Abstract

Scanning electron microscopy, coupled with energy-dispersive X-ray spectroscopy (EDS), is a powerful tool used in many scientific fields. It can provide nanoscale images, allowing size and morphology measurements, as well as provide information on the spatial distribution of elements in a sample. This study compares the capabilities of a traditional EDS detector with a recently developed annular EDS detector when analyzing electron transparent and beam-sensitive NaCl particles on a TEM grid. The optimal settings for single particle analysis are identified in order to minimize beam damage and optimize sample throughput via the choice of acceleration voltage, EDS acquisition time, and quantification model. Here, a linear combination of two models is used to bridge results for particle sizes, which are neither bulk nor sufficiently thin to assume electron transparent. Additionally, we show that the increased count rate obtainable with the annular detector enables mapping as a viable analysis strategy compared with feature detection methods, which only scan segmented regions. Finally, we discuss advantages and disadvantages of the two analysis strategies.

Key words: aerosol, electron microscopy, energy-dispersive X-ray spectroscopy, particle

(Received 9 April 2019; revised 4 November 2020; accepted 4 November 2020)

Introduction

Scanning electron microscopy (SEM) is capable of imaging samples with nanometer resolution, providing size and morphology information. When coupled with energy-dispersive X-ray spectroscopy (EDS), the method can also identify and quantify elements heavier than lithium (Hovington et al., 2016) and also by the detection of electron-excited characteristic X-rays. This makes SEM/EDS a powerful characterization tool applied in a broad range of fields including environmental (Laskin & Cowin, 2001; Laskin et al., 2006; Kandler et al., 2009; Kling et al., 2016), materials (Arepalli et al., 2004; Lee et al., 2004; Sathirachinda et al., 2010), and health sciences (Koh et al., 2008; Stebounova et al., 2011; Lee et al., 2015). The method is, however, subject to many sample specific uncertainties including morphological effects, sample–matrix interactions, and radiolytic beam sensitivity. Users therefore have to choose the optimal microscope settings prior to analysis, as well as the best-suited model and algorithms for quantification during data treatment. Here, microscopic settings include aperture size, spot size, acceleration voltage, and EDS acquisition time. Choices during data treatment mainly refer to the quantification model, though the quality of

background X-ray subtraction, deconvolution, and peak-fitting procedures also have a significant influence on the results (Newbury & Ritchie, 2013, 2014). These choices strongly affect the success of the analysis and the quality of results. Preferably, the choices should be evaluated on a case-by-case basis depending on sample and available equipment.

This study provides guidance on identifying settings and parameters of highest relevance for single particle analysis of thin electron transparent and beam-sensitive samples. Recommendations include the choice of acceleration voltage, EDS acquisition time, as well as the quantification model, where a comparison is made between Cliff–Lorimer (for electron transparent samples) and P/B-ZAF (for bulk samples). Here, a simple expression is used to bridge quantification results from particles in the size range transitioning from electron transparent to bulk sizes. The analyzed samples consist of NaCl particles in the size range 50–500 nm collected onto TEM grids. NaCl was chosen, firstly as it is present in many types of samples such as biological and environmental samples, and secondly because it is a beam-sensitive compound, like most alkali halides. This causes difficulties for standard EDS detectors due to degassing of halides from the NaCl surface upon extended beam exposure (Cazaux, 1995; Allen et al., 1998; Egerton et al., 2004).

Additionally, a comparison is made between a traditional side-mounted EDS 30 mm² silicon drift detector (SDD) and a newly developed annular EDS 4 × 15 mm² SDD situated between the pole piece and the sample. The new detector configuration achieves a much higher solid angle and significantly higher X-ray count rates than previous designs (Brodusch et al., 2018).

*Authors for correspondence: Kristian Mølhav, E-mail: krmo@dtu.dk, Anders Brostrøm, E-mail: abbl@dtu.dk

Cite this article: Brostrøm A, Kling KI, Hougaard KS, Mølhav K (2020) Analysis of Electron Transparent Beam-Sensitive Samples Using Scanning Electron Microscopy Coupled With Energy-Dispersive X-ray Spectroscopy. *Microsc Microanal*. doi:10.1017/S1431927620001464

This reduces the needed acquisition time without sacrificing counts. The increased count rate also makes it possible to map the entire imaged area within a reasonable timeframe, as opposed to limiting the EDS analysis to a selected subset of pixels — often referred to as feature analysis or particle detection (Teng et al., 2018). The study concludes with a comparison of mapping and feature analysis, highlighting available options and discussing the advantages and disadvantages of the two strategies when analyzing electron transparent samples.

Materials and Methods

Aerosol Generation and Collection

The sampled aerosol was generated with a constant output atomizer model 3076 (TSI, USA), which was operated at a backpressure of 2 bar. The atomizer generated aerosols from a solution of 1 g NaCl (purity $\geq 99.0\%$, Sigma-Aldrich, USA) in 500 mL nanopure water. From the atomizer, the aerosol was passed through two diffusion driers model 3062-NC (TSI, USA) installed with freshly dried silica gel, decreasing the relative humidity from 100 to less than 10%. The dried aerosol was sent into a small Plexiglas chamber of approximately 0.5 m³. A scanning mobility particle sizer (SMPS) was used to monitor the total number concentration in the chamber, which consisted of a differential mobility analyzer model 3082 (TSI, USA) and a condensation particle counter model 3776 (TSI, USA). The SMPS was operated in a low flow mode (0.3 L/min) with a sheath-to-aerosol flow ratio of 10. The aerosol was sampled from the chamber with a three-stage cascade impactor using a diaphragm gas pump model NMP 830 (KNF Neuberger, Germany). The aerosol was sampled at a flow rate of 0.76 L/min, giving impactor D_{50} values of 1.36, 0.59, and 0.073 μm for the three stages, respectively. Each stage was fitted with commercially available 400 mesh nickel TEM grids coated with a 25–50/1 nm Formvar/Carbon film (Electron Microscopy Sciences (EMS), USA). This allowed the atomized NaCl particles to be collected directly onto TEM grids and analyzed by SEM without additional preparatory steps. The appropriate particle coverage was achieved by sampling for 5 s at a total number concentration of approximately $3.5 \times 10^5 \text{ cm}^{-3}$, as measured by the SMPS. This fits well with the sampling recommendation of Broström et al. (2019). Particles were only observed on the lowest impactor stage, consistent with the expected 100–200 nm sizes, as the lowest stage collects particles with diameters from 73 to 590 nm (Broström et al., 2019).

Electron Microscope

The sampled grids were analyzed in a high vacuum mode with an Everhart-Thornley secondary electron detector in a Nova NanoSEM 600 (Thermo Fisher Scientific (former FEI), The Netherlands). The microscope is equipped with both XFlash 6|30 and XFlash FlatQuad (Bruker Nano, Germany) EDS detectors. The XFlash 6|30 (from here on referred to as XFlash) is a 30 mm² SDD delivering an energy resolution of 123 eV at Mn K α . The detector is placed 44 mm from the sample surface, with a take-off angle of 35°, and a corresponding solid angle of 0.0119 sr. The XFlash FlatQuad (from here on referred to as FlatQuad) is a 60 mm² retractable annular detector situated between the pole piece and the sample, with a take-off angle of 60°. The FlatQuad has an optimal sample to the detector distance of 3 mm (see Supplementary Material), which was used in this study,

corresponding to a solid angle of 0.95 sr. The FlatQuad is designed with a center hole for the incident electron beam to pass through and with four individual 15 mm² SDD quadrants mounted radially around it (see Supplementary Material), reaching an energy resolution of 126 eV at Mn K α . The four quadrants make the detector insensitive to potential sample shielding effects upon positioning and achieve a much higher solid angle than the XFlash. A schematic of the two detector configurations is shown in the Supplementary Material.

For all SEM/EDS analyses, the ESPRIT 2 software (Bruker Nano, Germany) was used. The necessary detector dead-times were estimated automatically by ESPRIT for each particle based on the measured counts per second (cps). For the XFlash, dead-times were almost exclusively 0% due to the relatively low cps. Measurements with the FlatQuad had a mean dead-time of $3.7 \pm 2.5\%$, though the largest particles had dead-times as high as 25%. Since the FlatQuad is situated directly above the sample, it is also exposed to high-energy electrons emitted from the sample. The FlatQuad is therefore equipped with a Mylar shield to absorb the incoming electrons. The thickness of the shield is increased with acceleration voltage, since more energetic electrons are emitted from the sample. The available thicknesses are 1, 1 + 2, and 1 + 6 μm Mylar for acceleration voltages below 6, 12, and 20 keV, respectively. Along with the high-energy electrons, a fraction of the low-energy X-rays will also be absorbed by the shield, depending on its thickness. As a result, the detection of X-rays is limited by an acceleration voltage in the high-energy region and by absorption from the Mylar shield in the low-energy region. These effects are accounted for automatically in the ESPRIT software-fitting procedures, but with the thickest shield it is not possible to quantify elements lighter than F. The FlatQuad detector was not inserted when performing EDS with the standard XFlash detector as it would block the X-rays leaving the sample.

The microscope was operated at acceleration voltages of 5, 10, or 20 keV, with an aperture size of 50 μm , and a spot size setting of 3.5, resulting in probe currents of 0.11, 0.16, and 0.19 nA for the three voltage settings, respectively. All SEM/EDS analyses were performed at 10k–12k on-screen magnification with pixel resolutions of approximately 7.1 nm/pixel.

To distinguish NaCl particles from the substrate, images were segmented using a fixed global threshold. The segmentation and EDS analysis were performed in two different ways for comparison:

- a) *Feature analysis*: Image segmentation is made prior to EDS analysis, in order to distinguish particles from the substrate and limit analysis to pixels recognized as particles. The beam is set to scan the entire area of each particle and acquisition times are set as livetimes, referring to the beam exposure time per particle regardless of its size.
- b) *Mapping*: An EDS map of the entire image is acquired and image segmentation is performed as a post-processing step. For maps, the acquisition time is set as a dwelltime, referring to the beam exposure per pixel, as particles are not yet distinguished from the substrate.

In both cases, spectra of all individual pixels within the contour of a single recognized particle were summed and analyzed as one. To remove the bremsstrahlung X-ray contribution from spectra, a background was fitted and subtracted before further analysis. The background fit was performed using the SEM fitting option available with the ESPRIT software, where areas suitable for fitting (areas without peaks) were identified automatically.

The fitting curve follows the shape of a bremsstrahlung X-ray background, taking into account the absorption of low-energy X-rays in the detector window and the electron shield. Generally, the automated post-processing algorithms functioned well, but in isolated cases, the procedures fitted the background to areas with peaks, or completely missed relevant peaks. Therefore, all individual particle spectra were manually inspected and critically evaluated on a case-by-case basis before trusting the results. Data handling, processing, and visualization of the EDS results were performed with Python 3.6.

Quantification Methods

Quantification models are needed to convert measured X-ray counts to concentrations in the form of mass or atomic percentages. There are several different quantification models available with commercial EDS software, though it is not always considered how big an influence the models have on the determined concentrations or which model to use for which samples.

The most common quantification method for EDS analysis is the P/B-ZAF method, which allows for a standardless, semi-quantitative analysis, while taking into account matrix interactions, such as fluorescence and absorption (Wendt, 1978; Wendt & Schmidt, 1978). It is used for bulk, polished, and homogeneous samples. However, for thin specimens, the X-ray-sample interaction is very limited and most matrix effects should be ignored as it can lead to unnecessary corrections. In this study, we compare results from P/B-ZAF to the Cliff-Lorimer model (Cliff & Lorimer, 1975), which is better suited for thin samples. Both methods are available in the ESPRIT software.

P/B-ZAF is a true standardless method as opposed to the standard-based ZAF (Armstrong & Buseck, 1975), where a reference sample with known composition is needed for quantification. Instead, P/B-ZAF uses the characteristics of the bremsstrahlung X-rays in the sample spectrum as a reference — hence using the spectrum background (B) as a reference for a given peak (P). The ESPRIT software determines the weight fraction of elements by iterative comparison between a standard database and the solutions to a set of nonlinear equations, taking the form of the following equation:

$$\left(\frac{P}{B}\right)_i = \frac{I_{i,\text{char}}}{I_{i,\text{br}}} = c_i * \omega_i * q_i * \frac{(Z*A*F)_{i,\text{char}}}{(Z*A)_{i,\text{br}}} \quad (1)$$

Where $I_{i,\text{char}}$ and $I_{i,\text{br}}$ are the number of characteristic and bremsstrahlung X-rays of an element i in a sample, while c_i is the mass fraction, ω_i is the fluorescence yield, and q_i is the relative emission rate of the given energy transition within element i . The Z , A , and F factors correct for sample matrix influences, where Z corrects for stopping power and backscattering effects which are atomic number-dependent (Duncumb & Reed, 1968), while the A and F factors correct for self-absorbing and fluorescence effects (Philibert, 1963; Reed, 1965).

For thin specimens, the produced X-rays have a low probability of interacting with the sample, making it possible to ignore absorption and fluorescence effects. The Cliff-Lorimer method relates the weight fractions (c) of elements A and B to the measured number of characteristic X-rays (I) by a Cliff-Lorimer factor K_{AB} using the following equation:

$$\frac{c_A}{c_B} = K_{AB} \frac{I_A}{I_B} \quad (2)$$

By convention Cliff-Lorimer factors are given relative to silica, so the factor for any two elements can be determined from the ratio of their silica factors using equation (3). For samples containing more than two elements, equations (3) and (4) are needed, which can be combined with equation (2) for the multi-element expression in equation (5):

$$k_{AB} = \frac{k_{AC}}{k_{BC}} \quad (3)$$

$$\sum_{i=A,B,C..} c_i = 1 \quad (4)$$

$$c_A = \frac{K_{ASi}*I_A}{\sum_{i=A,B,C..} K_{iSi}*I_i} \quad (5)$$

The Cliff-Lorimer factor K_{iSi} depends on both the instrument and element-specific factors, but it is independent of sample composition. The factors can therefore be determined for all instrument settings, either experimentally or through theoretical calculation. The experimental factors are more precise, reaching relative errors as low as 1%, while the theoretical factors can have systematic relative errors as high as 15–20% (Watanabe & Williams, 2006). However, multiple standard thin-film samples with known compositions are required to determine the experimental factors. The typical choice in most studies is the standardless P/B-ZAF and theoretical Cliff-Lorimer factors, and these are used in this work.

The two models can be used to quantify either bulk or electron transparent samples, but both fail in the particle size range transitioning from transparent to bulk sizes, as shown by Laskin et al. (2006). To overcome this issue, Kandler et al. (2018) recently proposed a simple method, where results from the two models are interpolated as a function of particle size. In the method, particles smaller than a threshold value ($1.5 \mu\text{m}$) are quantified by Cliff-Lorimer, while particles larger than another threshold value ($30 \mu\text{m}$) are quantified by P/B-ZAF. In the size range between the two values, particles are quantified with both models and the results are weighted based on particle size and summed. The method was developed based on samples of polished NaCl crystals analyzed at 20 keV. The proposed method is therefore only valid for NaCl at 20 keV, since lowering the acceleration voltage or analyzing a sample with a higher density than NaCl will shrink the interaction volume. As a result, smaller particles will act as bulk samples, making P/B-ZAF valid at sizes below $1.5 \mu\text{m}$. Here, it should be noted that a smaller interaction volume means that X-rays are produced closer to the particle surface, thereby reducing their sample interaction. Results from P/B-ZAF and Cliff-Lorimer quantification will therefore be more similar at small interaction volumes. Also, the difference between P/B-ZAF and Cliff-Lorimer results is lower for high-energy X-rays, which are not absorbed as readily as X-rays with energies below approximately 2 keV (Fletcher et al., 2011).

We propose an alternative interpolation method, where the depth of the interaction volume is considered when determining the P/B-ZAF and Cliff-Lorimer weights. We argue that particles larger than or equal to the depth of the interaction volume should be quantified as bulk samples using P/B-ZAF. In addition, we argue that particles with a size of half the depth of the interaction

volume should have equal weights for the two models. This gives a simple linear expression for the weights:

$$X = \begin{cases} D_p < D_i, & \frac{D_p}{D_i} * X_{\text{ZAF}} + \left(1 - \frac{D_p}{D_i}\right) * X_{\text{CL}} \\ D_p \geq D_i, & X_{\text{ZAF}} \end{cases} \quad (6)$$

Where X is the corrected concentration of a given element in the interaction volume, D_p is the estimated particle thickness, e.g. equivalent diameter, D_i is the depth of the interaction volume, while X_{ZAF} and X_{CL} are the element concentrations quantified using P/B-ZAF and Cliff-Lorimer, respectively. As discussed, the depth of the interaction volume is influenced both by sample characteristics and the acceleration voltage, but it can be estimated using the simple approach of Potts (1987):

$$D_i = \frac{0.1 * E_0^{1.5}}{\rho} \quad (7)$$

Here, E_0 is the acceleration voltage of the incident beam and ρ is the sample density (2.16 g/cm^3 for NaCl). Ideally, the weights should be determined from the interaction and particle volumes, accounting for particle geometry and adjusting according to the X-ray path within each individual particle relative to bulk and transparent samples. However, such assessments require complex calculations or simulations, as the size and shape of both particle and interaction volume are difficult to measure. A method using this approach was proposed by Ro et al. (2003), though it requires extensive Monte Carlo simulations and is thus not yet applicable for large datasets. The more simplistic correction based on the particle size and the interaction depth ratio is therefore proposed as a first-order correction, though it may introduce some bias. The bias may be significant for high aspect ratio particles, where the particle and interaction volume widths are also relevant for assessing the X-ray path within particles. Finally, some bias may result from scanning the beam across particles, as opposed to stationary measurements at the particle center. This will

generally reduce the mean X-ray path within particles, as X-rays can be generated near the particle surface or edge during a scan.

Results and Discussion

A series of images was acquired of the NaCl samples at 5, 10, and 20 keV. The ESPRIT software *feature analysis* was used for automated image acquisition, image segmentation, and subsequent EDS analysis of the individual particles. At each voltage, three different image/EDS procedures were performed with particle lifetimes of 1, 5, and 15 s, respectively. For the 15 s lifetime setting, the total number of particles for EDS analysis was limited to 100, in order to reduce the overall acquisition time. These analyses were performed both with the XFlash and FlatQuad detectors, but in different areas of each sample to avoid accumulated beam damage. A table of all 18 setting combinations is shown in the Supplementary Material, along with nine SE images of the areas used for EDS analysis with the XFlash detector. Results from a feature analysis performed at 20 keV with the FlatQuad using 15 s lifetime is shown in Figure 1.

From the spectrum, it is seen that many elements apart from pure NaCl are detected, including Al, Si, Sn, Cr, Fe, and Cu. These elements can be attributed to the setup as transmitted or stray electrons hit the sample holder, detector housing, or microscope chamber. A substantial carbon peak is also visible, which originates from the Carbon/Formvar substrate and to a lower extent from potential volatile organic compound contamination. The spectrum was quantified using Cliff-Lorimer, which gave the atomic percentages presented in Table 1. Here, oxygen was included in the fitting procedures, but was deconvoluted prior to determining atomic percentages, as it has a very low X-ray yield, making it difficult to quantify. Oxygen concentrations are therefore often determined based on stoichiometry rather than the X-ray count (Newbury & Ritchie, 2014).

As seen from Table 1, the dominating element is C, while the two second most abundant elements are Na and Cl, which fits well with the expected pure NaCl particle on a carbon substrate. Substantial concentrations are also detected of Ni, originating

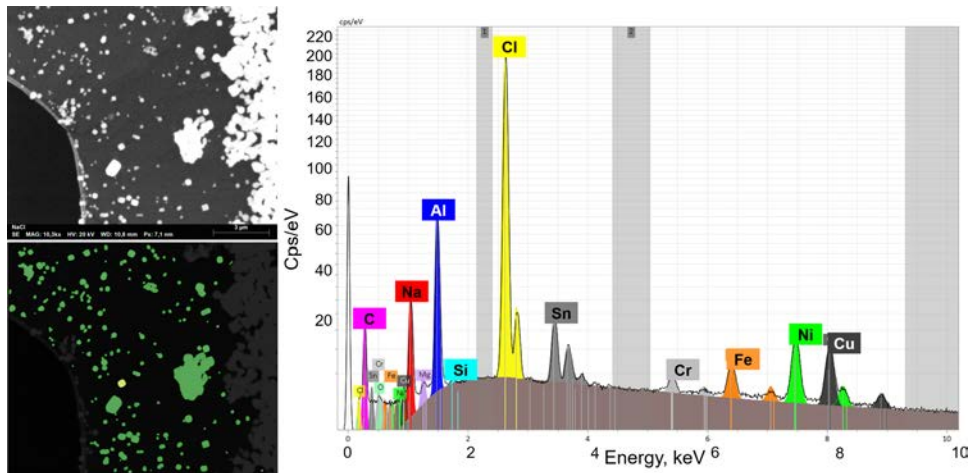


Fig. 1. Top left: SE image of the NaCl sample at 20 keV. Bottom left: Segmented SE image, where all pixels categorized as particles are marked in green. Right: the EDS spectrum of the particle marked in yellow on the segmented SE image. The original spectrum is in black, while the fitted background is in dark grey at the bottom. The areas used for fitting the bremsstrahlung background are marked as light gray columns. Fitted element peaks are presented in various colors with the name of the element written above the primary peak. Element-specific emission lines are also presented as thin vertical lines in the bottom of the spectrum using the element respective colors, with the height of the line indicating its relative intensity. X-rays are binned into 5 eV energy bins, and the y-axis is square root-scaled for easier visualization.

Table 1. Table of Element Quantification Results from the EDS Spectrum in Figure 1 Along with Errors Estimated by the ESPRIT Software.

Element	At. No.	X-ray Count	Atomic %	Abs. Error, % (1 sigma)	Rel. Error, % (1 sigma)
C	6	14,807	68.22	2.16	3.17
Na	11	27,449	10.73	0.35	3.26
Cl	17	312,575	7.72	0.25	3.19
Ni	28	3,096	5.37	0.56	10.34
Al	13	77,223	5.31	0.18	3.36
Cu	29	27,879	0.81	0.03	4.03
Mg	12	4,953	0.66	0.04	6.40
Sn	50	41,905	0.61	0.70	10.70
Fe	26	17,299	0.35	0.02	5.62
Cr	24	8,191	0.14	0.01	10.09
Si	14	1,572	0.07	0.02	26.29
O	8	15	—	—	—

Oxygen was included in the fitting procedures during quantification, but was deconvoluted before determining mass and atomic concentrations as the oxygen signal is highly uncertain in EDS.

from the Ni TEM grid, and Al, originating from the microscope and the sample holder, which is made of aluminum. The aluminum signal could thus be reduced by installing, e.g. a carbon-based

object (shield) underneath the sample to absorb transmitted electrons, or by exchanging the sample holder material. The remaining elements were identified as trace elements, making up less than 1 at % each, and environmental particles with these components would therefore still be distinguishable. It should, however, be noted that the absorption of low-energy X-rays by the thick Mylar shield necessary at 20 keV makes the quantification of light elements such as C highly uncertain. This uncertainty is not captured in the error estimates of the ESPRIT software in Table 1.

Detector Comparison

A common challenge in EDS analysis is the number of counts needed to obtain a sufficient precision. For example, 10k, 2.5k, and 0.4k counts in a peak are needed to reduce the relative uncertainty of the element fraction to 1, 2, or 5%, when based on counting statistics alone. For relatively low solid angle detectors such as the XFlash, it is challenging to reach peak counts higher than 1000 within the short acquisition times necessary for beam-sensitive compounds. However, when positioning detectors between the pole piece and the sample as for the FlatQuad, a much greater solid angle is achieved, increasing the X-ray count rate substantially. To demonstrate the outcome of the two detector designs, the EDS spectra of NaCl particles with an equivalent circular diameter (D_{eq}) of approximately 100 and 500 nm at 5, 10, and 20 keV, using either 1 or 15 s livetime for both the XFlash and FlatQuad detectors, are presented in Figure 2. The spectra are presented without background subtraction, which is why the 5 keV spectra drop to zero counts at 5 keV, as the incident

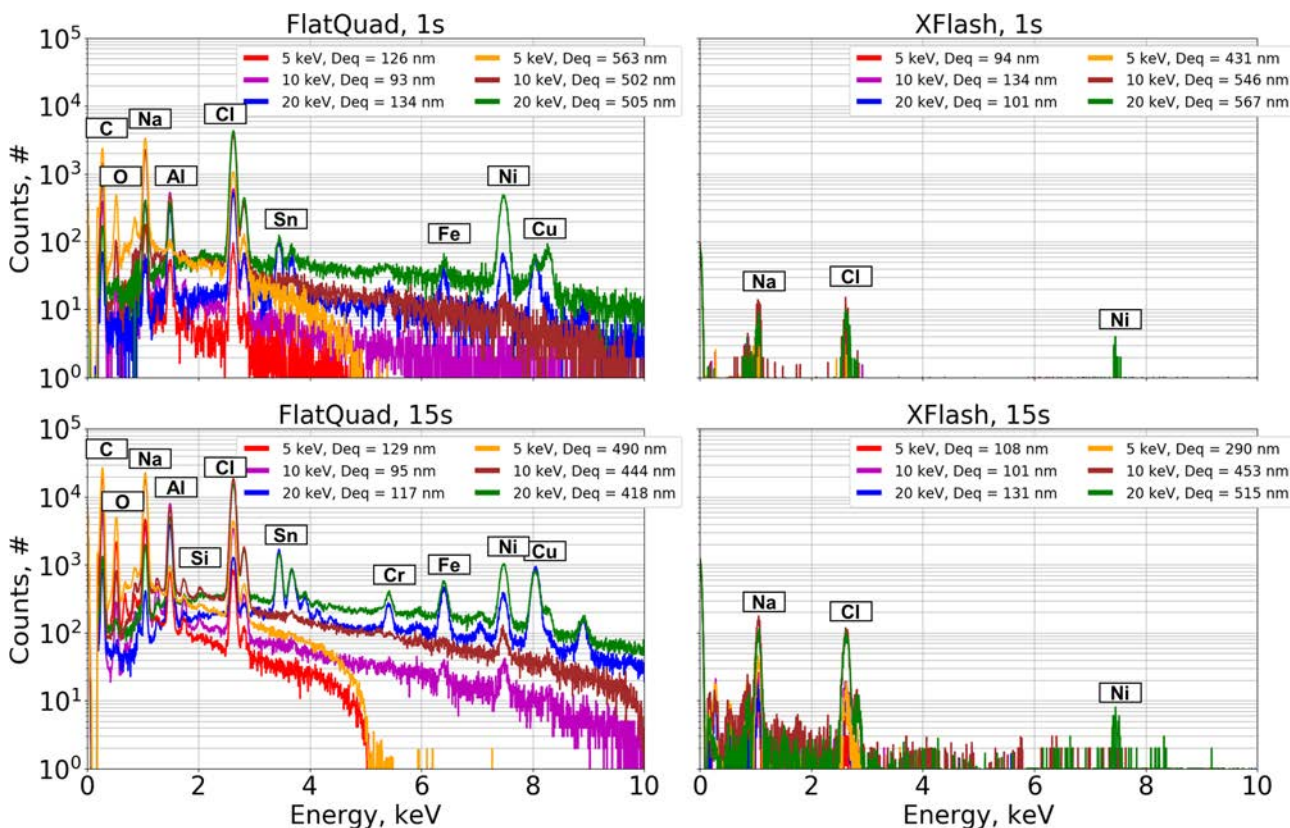


Fig. 2. EDS spectra of NaCl particles with D_{eq} of approximately 100 and 500 nm acquired at 5, 10, or 20 keV, using either 1 (top row) or 15 s (bottom row) livetime for the FlatQuad (left column) and the XFlash (right column). The D_{eq} of the corresponding NaCl particles are shown in the legend. Y-axis is in log scale, showing the total number of X-ray counts during the entire acquisition period, for each 5 eV energy bin.

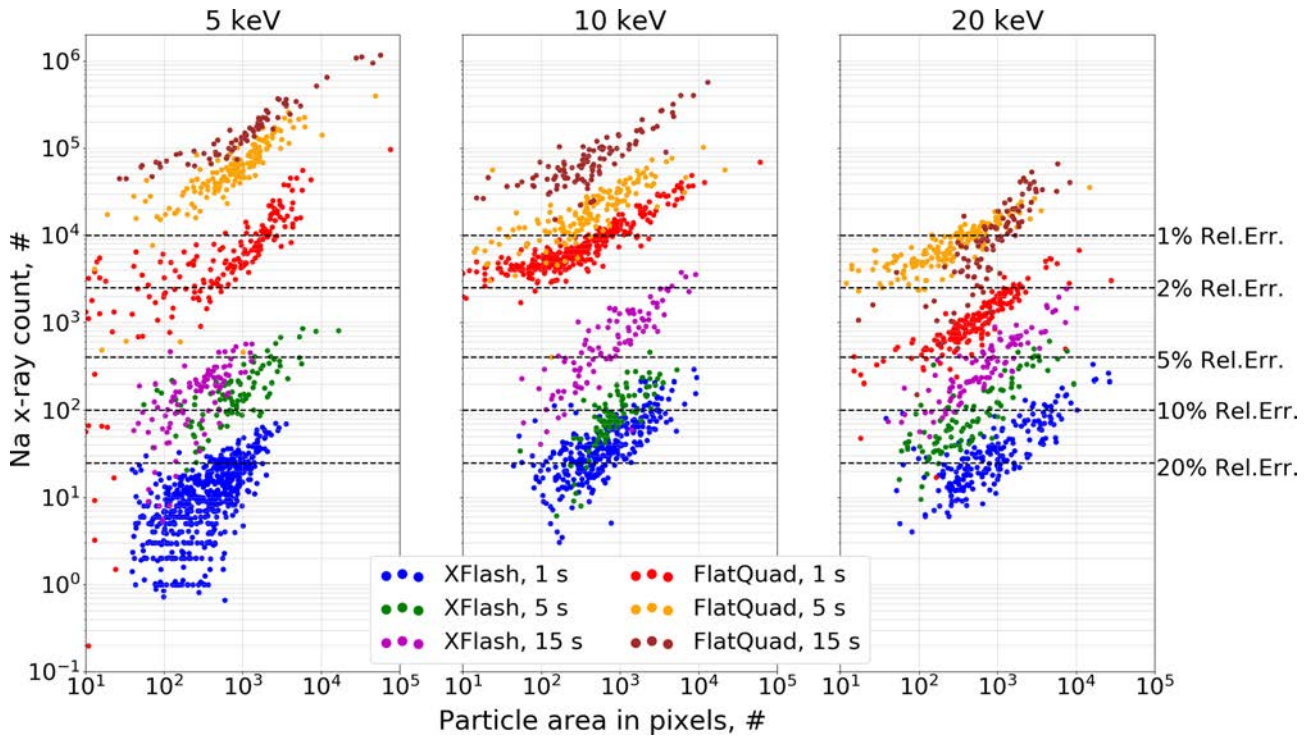


Fig. 3. Total X-ray counts in the Na peak for each individual particle spectrum after background subtraction, for all combinations of acceleration voltage, livetime, and detector, plotted against particle size in pixels. The dashed black lines mark 1, 2, 5, 10, and 20% relative error based on counting statistics as \sqrt{N} , where N refers to the number of detected Na X-rays. The pixel size was approximately 7.1 nm for all images.

electrons cannot generate X-rays with energies higher than the beam. An overview table showing voltages, lifetimes, particle sizes, and the integrated X-ray count from 100 eV to the incident beam for each spectrum in Figure 2 can be found in the Supplementary Material.

As seen from Figure 2, the number of counts in the FlatQuad spectra are several orders of magnitude higher than for the XFlash when operating at similar conditions. As a result, the FlatQuad spectra display clearly distinguishable element peaks containing thousands of counts, while the XFlash can barely detect the major components Na and Cl at 1 s livetime. Furthermore, the number of bremsstrahlung X-rays are limited for the XFlash when using short acquisition times, which complicates background fitting and subtraction procedures.

To investigate which settings allow for low relative errors compared to the acquisition time, the number of X-rays detected in the Na peak of each particle EDS spectrum are plotted against the particle area in pixels in Figure 3. The plot includes all combinations of acceleration voltage, livetime, and detector type. All elements listed in Table 1 were included in the identification list, and the Na X-ray counts were determined after background subtraction. A boxplot of the Na X-ray count for the two detectors, which have been normalized by particle area and livetime, can be found in the Supplementary Material.

From Figure 3, it is seen that the number of X-ray counts in the Na peak is highly dependent on the particle size, as more electrons will pass through smaller particles with zero loss, resulting in lower X-ray yields. Here, it should also be noted that though EDS livetime is constant, the dwelltime is not. This means that small particles consisting only of a few pixels are scanned more intensively during the same livetime, making them particularly susceptible to beam damage.

It is furthermore seen from Figure 3 that an increase in the acceleration voltage does not necessarily result in higher X-ray counts for electron transparent samples, as would be expected for most bulk samples. A part of the reduced counts may result from a higher absorption of the low-energy Na K α X-rays (1.040 keV), when traversing the thicker detector shield at 20 keV relative to 5 keV. This reduction is, however, accounted for in the quantification algorithm of the Esprit software. The lower counts may also result from the increased penetration depth of the more energetic electrons, which, for thin samples, means that more electrons are transmitted without detectable interaction (Friel & Lyman, 2006). The change in the interaction volume was exemplified by performing Monte Carlo simulations of electron interaction with flat bulk NaCl samples, using Casino v3.3 (Demers et al., 2011). Here, a maximum penetration depth of approximately 0.4, 1.3, and 4 μm , respectively, was found when simulating 10,000 electron trajectories at acceleration voltages of 5, 10, and 20 keV. Images from the simulation are shown in the Supplementary Material. As the average equivalent diameter of the NaCl particles analyzed in this study is 215 ± 205 nm, the 10 and 20 keV settings will have a significantly higher fraction of zero loss electrons. This effect is, however, mitigated slightly by the corresponding increase in probe current, which rises from 0.11 to 0.16 and 0.18 nA for 5, 10, and 20 keV, respectively. The net effect is an inverse relation between X-ray count and voltage, with the highest counts obtained at 5 keV, though the effect is not visible for the low counts of the XFlash detector.

Overall, it is clear that the livetime needed to ensure relative errors below e.g. 2% and can be decreased by orders of magnitude when using the FlatQuad detector compared to the XFlash. Even the 15 s livetime for the XFlash is approximately an order of

314
315
316
317
318
319
320
321
322
323
324
325
326
327
328
329
330
331
332
333
334
335
336
337
338
339
340
341
342
343
344
345
346
347
348
349
350
351
352
353
354
355
356
357
358
359
360
361
362
363
364
365
366
367
368
369
370
371
372
373
374
375

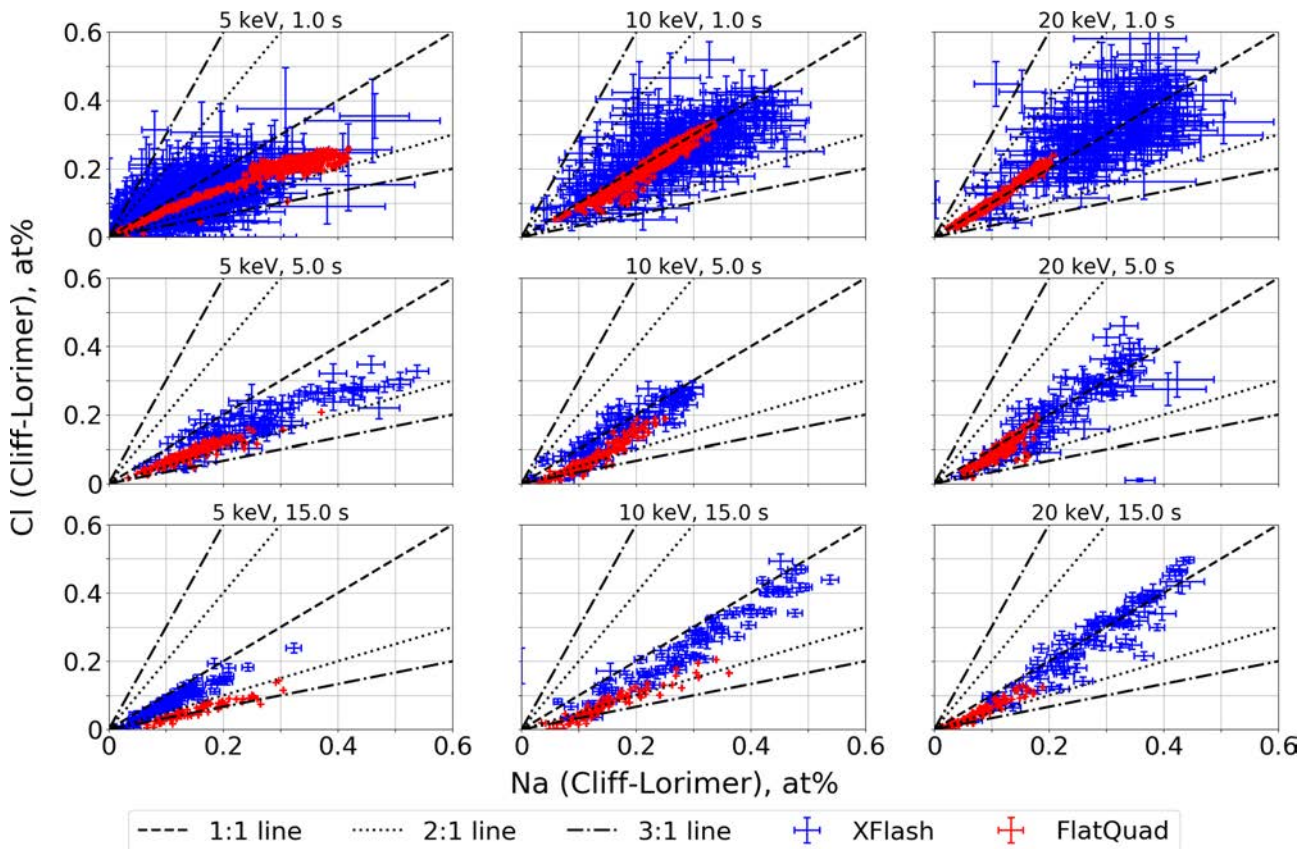


Fig. 4. Plot of Na at% against Cl at% for the XFlash (blue) and FlatQuad (red) quantified with Cliff-Lorimer. Error bars were determined based on counting statistics as \sqrt{N} from the number of X-ray counts in the Na or Cl spectrum peaks. Lines corresponding to ratios of 1:1, 2:1, and 3:1 have also been plotted as a reference.

magnitude lower in counts, compared with the FlatQuad at 1 s livetime. This reduces the overall EDS analysis time from hours to minutes and opens for new possibilities such as mapping of the entire image, rather than limiting EDS to pixels recognized as particles.

For comparison of the quantified results, all spectra were analyzed using the Cliff-Lorimer model, and the resulting Na and Cl at% were plotted against each other for all settings in Figure 4. Here, it should be noted that the higher Na and Cl concentrations measured with the XFlash compared to the FlatQuad are partly due to the detector and sample holder configuration. The XFlash is located slightly behind the bulk sample holder and is therefore shielded from X-ray emissions below the sample. In contrast, the FlatQuad is mounted directly above the sample, thereby detecting most X-rays emitted from below, resulting, e.g., in higher Al counts and a corresponding reduction in the relative Na and Cl at%.

When comparing results from the two detectors, it is clearly seen that the low counts of the XFlash detector give major uncertainties at the 1 s livetime, whereas the FlatQuad detector provides consistent results, following clear trends. As the livetime is increased, the uncertainties of the individual XFlash data points are reduced, but they still display a larger spread than for the FlatQuad. The higher consistency of the FlatQuad results reveals systematic deviations from the 1:1 line, which are partly obscured in the XFlash results. These deviations are related to beam damage and quantification model, which will be discussed in the following sections.

Beam Sensitivity

The influence of beam damage is seen in Figure 4, when comparing plots in the same column. Here, the same microscope settings are used, but the beam exposure is varied. Upon longer exposure, the particle's composition shifts from values close to the 1:1 line at the 1 s livetime towards the 2:1 and 3:1 lines at 5 and 15 s livetimes. All observed shifts correspond to an enrichment in Na relative to Cl, which is consistent with the loss of halides upon beam radiation, as reported in the literature (Cazaux, 1995; Allen et al., 1998; Egerton et al., 2004).

It is furthermore seen that the beam damage is most severe at 5 keV, where the Na/Cl ratio shifts from the 1:1 line at 1 s livetime to the 1:3 line at 15 s. In comparison, the ratio only shifts to the 1:2 line at 20 keV. The smaller shift is due to a higher number of transmitted electrons at 20 keV compared with 5 keV. At 5 keV, the majority of the interaction volume is within, e.g., a 300 nm particle, which results in a higher degree of beam damage. However, a shift to the 1:2 line at 20 keV and 15 s livetime still indicates a significant beam influence upon the extended livetime. This can also be observed directly when comparing images before and after EDS analysis, which can be seen in Figure 5, where the NaCl sample analyzed at 20 keV with 15 s livetime is shown.

Figure 5 clearly shows the severity of beam damage for NaCl, with most of the particles transformed to craters after the EDS analysis. Even particles of a few hundred nm have almost completely disappeared during the 15 s livetime, while many of the smaller particles are no longer visible. It is therefore obvious

376
377
378
379
380
381
382
383
384
385
386
387
388
389
390
391
392
393
394
395
396
397
398
399
400
401
402
403
404
405
406
407
408
409
410
411
412
413
414
415
416
417
418
419
420
421
422
423
424
425
426
427
428
429
430
431
432
433
434
435
436

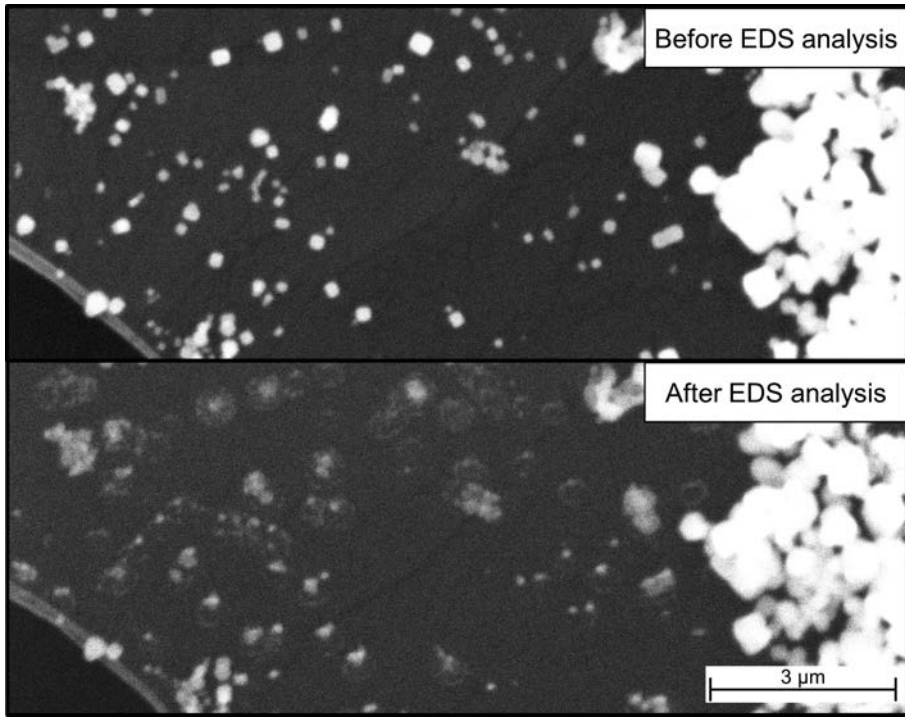


Fig. 5. SE images of NaCl particles before (top) and after (bottom) EDS analysis performed at 20 keV with a particle lifetime of 15 s. Pixel resolution was 7.1 nm.

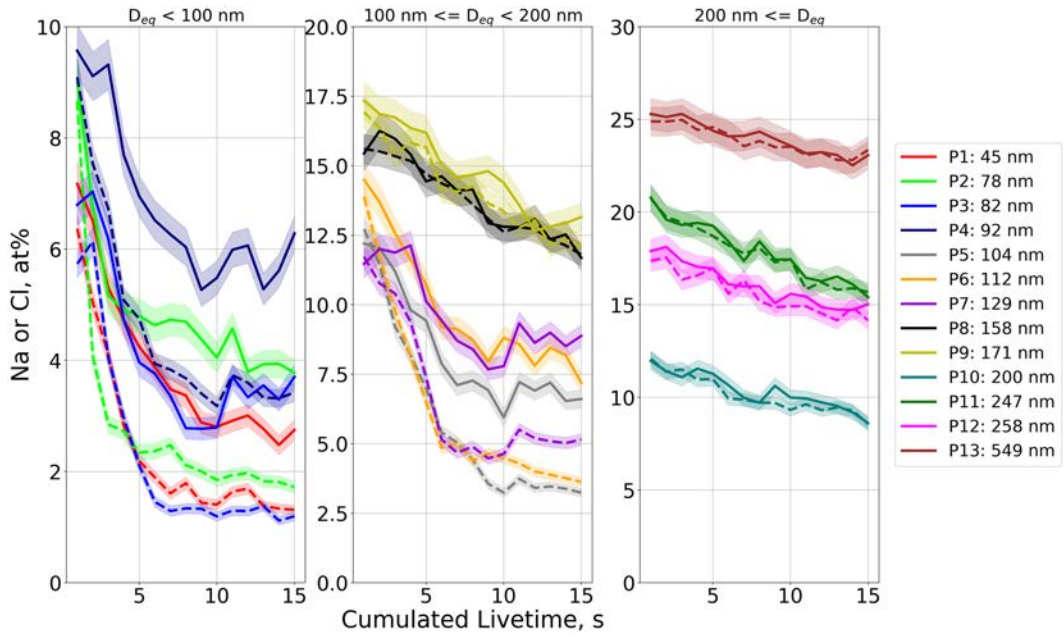


Fig. 6. The Na (solid lines) and Cl (dashed lines) atomic percentages from 15 consecutive EDS measurements at 10 keV for a selection of 13 NaCl particles with sizes ranging from approximately 50 to 550 nm. The Cliff-Lorimer model was used for quantification and the shaded areas represent uncertainties determined from counting statistics (\sqrt{N}). Particle sizes are reported as equivalent circular diameters. It should be noted that the y-axis is scaled differently in the three plots.

that beam exposure can alter the shape, size, and elemental composition of a beam sensitive sample.

To further investigate the beam effects, a series of 15 consecutive EDS measurements with a 1 s lifetime were conducted at 10 keV in the same area of the sample. This made it possible to quantify the Na and Cl concentration of selected particles with

a range of sizes and plot them as a function of beam exposure, as seen in Figure 6.

From the three plots in Figure 6, it is seen that the Na and Cl concentrations are similar at the 1 s lifetime for all particles, consistent with the expected 1:1 ratio. However, as the beam exposure continues, both the Na and Cl content decrease, regardless of the

500
501
502
503
504
505
506
507
508
509
510
511
512
513
514
515
516
517
518
519
520
521
522
523
524
525
526
527
528
529
530
531
532
533
534
535
536
537
538
539
540
541
542
543
544
545
546
547
548
549
550
551
552
553
554
555
556
557
558
559
560

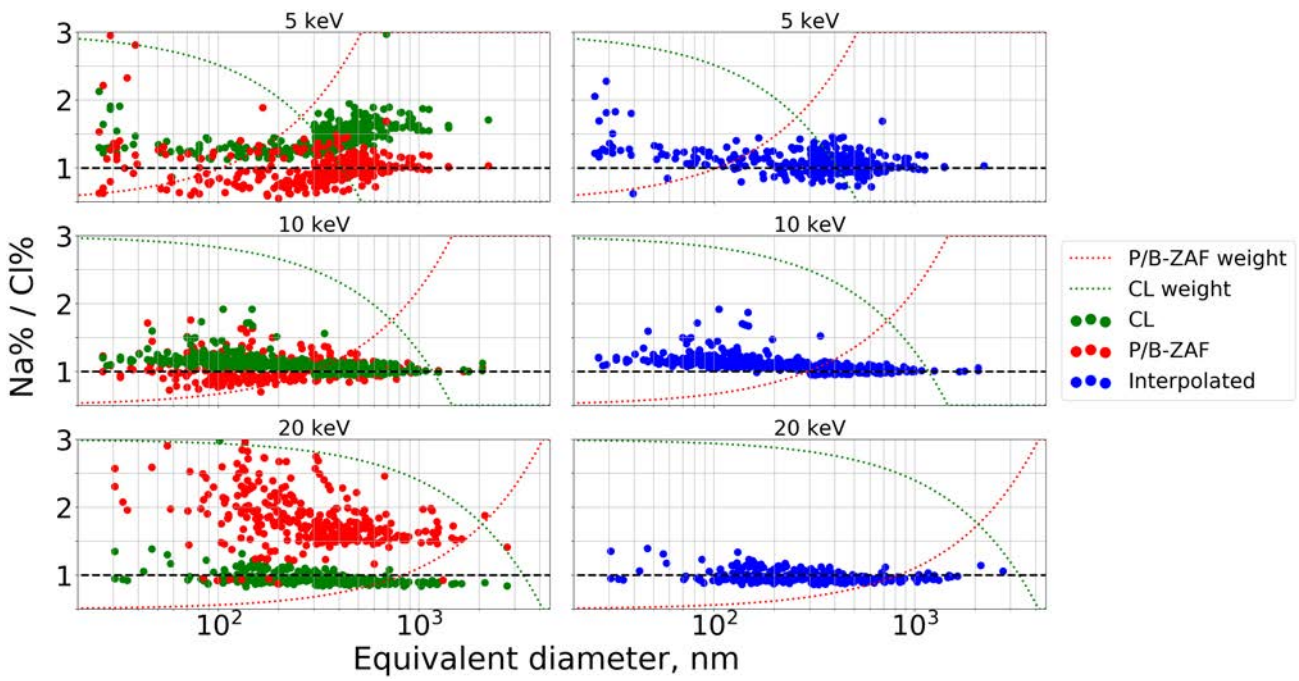


Fig. 7. Ratios of Na/Cl (at%) quantified by P/B-ZAF (red) and Cliff–Lorimer (green) plotted against particle equivalent diameter at 5 keV (top), 10 keV (middle), and 20 keV (bottom). The data points in blue are the Na/Cl ratios interpolated by the proposed algorithm in equation (6). The dotted red and green lines correspond to the size-dependent weights of the algorithm, which scale from 0 to 1. The crossing point of the red and green dotted lines is at half the interaction depth, while the point where they reach 1 and 0 is at the interaction depth for the given voltage and density (2.16 g/cm^3 for NaCl).

particle size. The relative decrease is most severe for particles smaller than 150 nm. These particles experience a reduction to approximately half their original concentration during the 15 s exposure, corresponding to a drop of 4–6 at% in Na and Cl. Larger particles show a similar decrease, but as their initial concentration is higher, the relative drop is smaller. It is furthermore seen that Cl is depleted faster than Na in particles below 150 nm, while it follows the Na depletion in larger particles. The different depletion rates could be related to the higher surface to volume ratio in small particles, causing a faster Cl evaporation. However, when comparing the results of Figures 4 and 6, it is seen that particles of all sizes shift in the Na/Cl ratio when exposed continuously for either 5 or 15 s, while only the smaller particles experience a shift when exposed repeatedly for 1 s. This indicates that the local radiolysis or temperature is more severe for the continuous exposure compared to the 15 consecutive exposures, where radical concentrations and temperatures are allowed to drop between measurements.

Finally, it is seen from Figure 6 that the decrease in concentration is most severe during the first few seconds of beam exposure, highlighting the need for short EDS lifetimes when working with small beam-sensitive particles. This is, however, challenging for detectors with a relatively low solid angle, as their count rates require longer lifetimes in order to reach a sufficient number of counts.

Quantification Method

As discussed previously, the choice of the quantification model also influences the quality of EDS results. This can be seen when comparing the FlatQuad concentrations in the top row plots of Figure 4, where beam damage is minimal. Here, the Na/Cl ratios fall directly on the 1:1 line at 20 keV, whereas the ratios at 5 keV start to deviate for higher Na and Cl concentrations, which

were measured from the largest particles. The observed deviation results from the Cliff–Lorimer model, which assumes that there is a minimal sample interaction. However, the lower electron energy at 5 keV shrinks the interaction volume to a depth of approximately 500 nm, compared with 4,000 nm at 20 keV. As a result, the largest particles [$D_p > D_i$, equation (7)] in this study will behave as bulk samples rather than electron transparent, making P/B-ZAF better suited for quantification, though Cliff–Lorimer is still needed for the smallest sizes [$D_p << D_i$, equation (7)]. To illustrate the difference between the two models, their Na and Cl quantification results from the 1 s livetime FlatQuad measurements at 5, 10, and 20 keV (Figure 4) are plotted as Na/Cl ratios against particle size in Figure 7. Here, results from the proposed interpolation model in equation (6) are also presented, along with the weights used for correction (scaling from 0 to 1).

At 5 keV, the Cliff–Lorimer model slightly overestimates the Na/Cl ratios for particle sizes smaller than 200 nm, which could be the result of beam damage. However, as the particle size increases, the Cliff–Lorimer model predicts a rise in the Na/Cl ratio, resulting in values further from unity. This shows that the Cliff–Lorimer model is ill suited for the quantification of the largest particle sizes, which act as bulk samples. The P/B-ZAF model reports highly varying Na/Cl ratios at small particle sizes, ranging from 0.5 to approximately 1.5. At larger sizes, the ratios converge towards unity consistent with the transition from transparent to bulk sizes, which should make the P/B-ZAF model more precise.

At 10 keV, both the Cliff–Lorimer and the P/B-ZAF models report Na/Cl ratios close to unity for all particle sizes, despite an expected discrepancy. This may, however, be different for samples other than NaCl, where sample interactions are different.

At 20 keV, all particle sizes are significantly smaller than the depth of the interaction volume. As a result, the P/B-ZAF model overcompensates for matrix interactions, resulting in Na/

Cl ratios that are 2–3 times higher than the actual. In contrast, the Cliff–Lorimer model reports ratios close to unity for all sizes, though a systematic decrease is observed at the largest particle sizes. This indicates the beginning of a transition from transparent to bulk sizes, which is consistent with the observations of Kandler et al. (2018).

Results from the proposed interpolation are shown in the plots in the right-hand side of Figure 7. At 5 keV, the interpolation presents the more precise Cliff–Lorimer ratios at small sizes, but corrects for the increase observed at larger sizes, as the P/B-ZAF model is weighted heavier. At 10 keV, both the P/B-ZAF and Cliff–Lorimer ratios are close to unity at all sizes and the interpolation therefore resembles both. At 20 keV, all particles are significantly smaller than the interaction volume, and the interpolation is largely based on the Cliff–Lorimer results. However, it is seen that the interpolation corrects for the slight decrease in the Cliff–Lorimer ratios at larger sizes, by introducing the weighted P/B-ZAF results. Finally, it is seen that some degree of beam damage is observed for the smallest particle sizes, where all of the interpolated values are slightly above unity. This effect is again most severe at 5 keV and least so at 20 keV, consistent with the observations in Figure 4. Overall, the Na/Cl ratios determined with the interpolation are close to unity for all particle sizes and all acceleration voltages used in this study. Additional research is, however, needed to investigate its use for larger particle sizes, and for samples other than NaCl, potentially with different shapes.

Comparison of Mapping and Feature analysis

The increased count rate and the following decrease in acquisition time achievable with the FlatQuad detector opens the possibility for using mapping as opposed to feature analysis. Here, the two techniques are compared and their advantages and disadvantages are discussed.

Feature Analysis

Feature analysis can greatly reduce the time needed to perform EDS analysis, as only pixels recognized as particles are taken into account. The majority of the image (all pixels not recognized as particles) is thus excluded from the analysis. This is a major advantage when using low solid angle detectors that require a long exposure time to reach sufficient X-ray counts. Feature analysis also makes it possible to set a fixed EDS livetime per particle, set a minimum number of X-ray counts needed per particle, or set a fixed pixel dwelltime. Minimum count requirements can be used to ensure sufficient X-ray counts from particles of all sizes or composition, while a fixed pixel dwelltime can be used to minimize beam damage for sensitive samples. However, the image segmentation can be difficult and often yields poor results, especially when automated imaging is used for analysis of multiple areas or images in the sequence. A poor segmentation can result in a large number of substrate areas misclassified as particles, which increases the overall analysis time extensively, and in worst case, require the automated analysis to be aborted or discarded. A new image segmentation can be made in case of poor results, but as the EDS analysis was limited to the predetermined pixels, the new segmentation can only give physical parameters and not composition. Feature analysis also has significant weaknesses, when sample drift is not accounted for (e.g. by drift correction). Since image segmentation is performed prior to EDS analysis, sample drift can cause the beam to completely or

partially miss targeted particles, or mix EDS results from a neighboring area into the segmented particle, which is not apparent for the user. It can be very challenging to determine whether drift occurred during the analysis, unless SE images are acquired both before and after analysis and compared, and even then, charging differences may make this irreproducible. Ultimately, the entire analysis may need to be repeated, which can be an issue for beam-sensitive samples, as the previous SEM/EDS analysis may have altered the shape or composition of already analyzed particles, hence requiring a new sample area.

Mapping

Mapping generally takes longer to perform compared to feature analysis, as all pixels are included in the EDS analysis. Furthermore, it is only possible to use fixed pixel dwelltimes, as particles are not yet distinguished from the substrate. This results in very low beam exposure for small particles, making their determined elemental compositions highly uncertain. However, unlike feature analysis, mapping allows for offline image segmentation, since both SE and EDS signals are stored individually for all pixels. This opens up for multiple post-processing options, such as segmentation based not only on the SE image, but also on elemental maps generated from EDS data. Images and individual particles can therefore be visually screened for specific elements of interest. Additionally, the element distributions available in maps provide information on the heterogeneity in the mixing state of individual particles. This information is highly useful when classifying particles, since primary particles of different composition are easily distinguished in EDS, even if they exist in agglomerated forms, consisting of several different primary particles. Finally, mapping makes it possible to subtract the EDS contribution originating from the sample substrate, from each individual particle, as will be demonstrated later.

Dwelltime and Livetime Comparison

For a fixed pixel dwelltime, small particles consisting of only a few pixels will have very low beam exposure, yielding low X-ray counts. This is exemplified in Figure 8, where the Na X-ray count of individual particles is plotted against their area in pixels, for particles analyzed by feature analysis with 1 s livetime and for four maps with a pixel dwelltime of 64, 128, 256, and 512 $\mu\text{s}/\text{pixel}$, respectively. Each analysis was performed in different areas of the sample to avoid beam damage. The acquisition times of the maps were approximately 4, 7.5, 15, and 30 min, respectively, while the feature analysis was completed in approximately 3 min with 142 particles in total (and some dead-time in between particles).

It is seen in Figure 8 that the X-ray count in the Na peaks is much higher for small particles when using feature analysis with a fixed particle livetime, compared with the fixed pixel dwelltime applied in mapping. This is because the overall exposure time is fixed for feature analysis but decreases with size for mapping. The particle X-ray yield in mapping is therefore highly particle size-dependent, while size is less significant for fixed livetimes where all particles are exposed for the same amount of time. However, the X-ray yield with fixed livetimes is still influenced by the particle volume, which determines the fraction of incoming electrons that interact with the particle (assuming the same elemental composition). Since volume is roughly proportional to the area, the fixed livetime X-ray yield still has some size dependency. This is particularly evident at small sizes where many electrons are transmitted, while it is insignificant for larger sizes where the majority of the interaction volume is

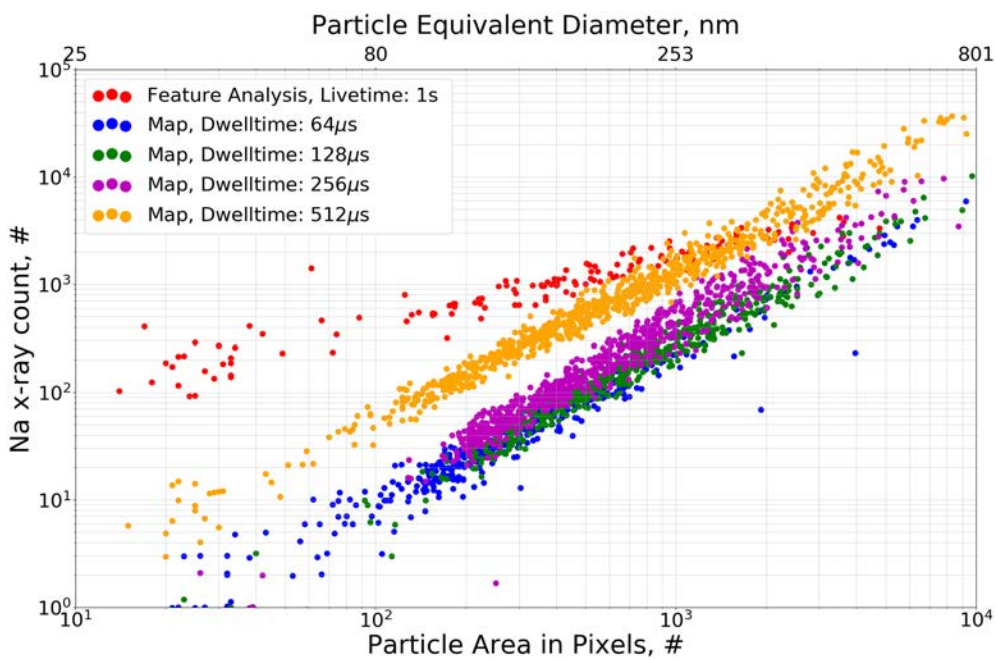


Fig. 8. Total X-ray count in the Na peak for individual particle EDS spectra after bremsstrahlung background subtraction for a feature analysis with the 1 s livetime and four EDS maps with pixel dwelltimes of 64, 128, 256, and 512 μ s. Particle sizes are displayed as an area in pixels on the bottom x-axis and as equivalent circular diameters in nm in the top x-axis, both in a logarithmic scale. All analyses were performed at 10 keV and at 10k magnification, corresponding to a pixel size of 7.1 nm.

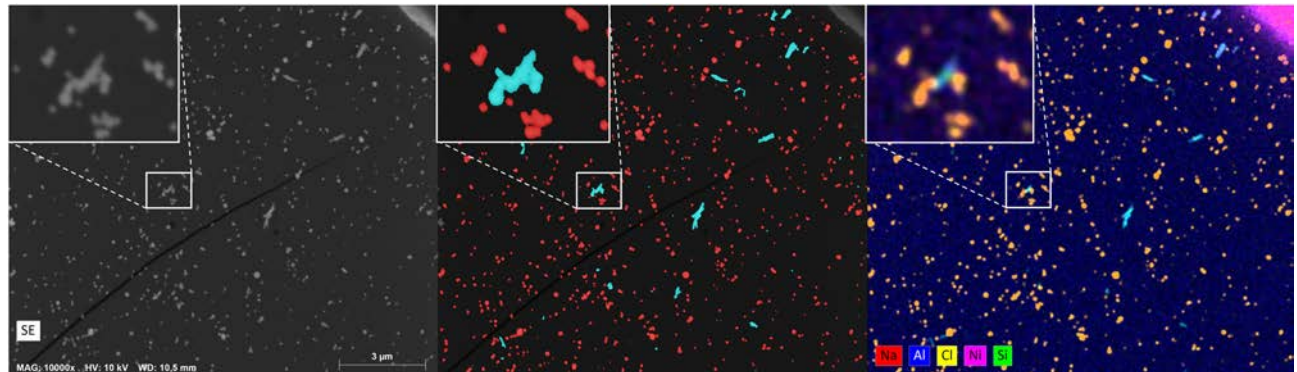


Fig. 9. (left) SE image of an area of the NaCl sample contaminated with aluminosilicate particles. (middle) Classified image from a feature analysis with a livetime of 1 s, where particles with Na + Cl at% higher than 4 are shown in red, while particles with Si at% higher than 2 are cyan (overwriting the Na + Cl criteria). (right) Overlaying element maps displaying X-ray counts for Na (red), Al (blue), Cl (yellow), Ni (magenta), and Si (green). The maps were acquired with a pixel dwelltime of 256 μ s. Insets depict a zoom-in on the same agglomerate particle consisting of NaCl particles and an aluminosilicate fiber.

within the particle. If this volume dependency is ignored, the particle size where mapping yields higher counts than fixed livetimes can be calculated, as presented in the Supplementary Material. For a feature analysis with the 1 s livetime, the crossing points are at particle sizes of approximately 15,600, 7,800, 3,900, and 1,950 pixels for map dwelltimes of 64, 128, 256, and 512 μ s, respectively. For the images presented here, which have a pixel resolution of 7.1 nm/pixel, these sizes correspond to equivalent circular diameters of approximately 1,000, 700, 500, and 350 nm for the four dwelltimes, respectively. The particle sizes at the crossing points can be reduced by performing the map analysis at higher magnification, thereby increasing the number of pixels within each particle. This will, however, reduce the area covered in each image and thereby increase the overall analysis time if the same area is to be

analyzed. This shows that the feature analysis with a fixed livetime is better suited for EDS analysis of small particles compared to maps with a fixed pixel dwelltime. It should, however, be noted that the smaller particles are more sensitive to sample drift and subject to intense beam radiation for fixed livetimes, and the method is therefore less suited for beam-sensitive samples.

Classification of Particles

The individual pixel data in maps enables the visualization of the internal particle mixing state, as opposed to the integrated elemental composition obtained by feature analysis. Interpreting the visualized data from elemental maps makes it possible to distinguish fully mixed particles from aggregates and agglomerates. An area on the NaCl sample contained trace contamination by

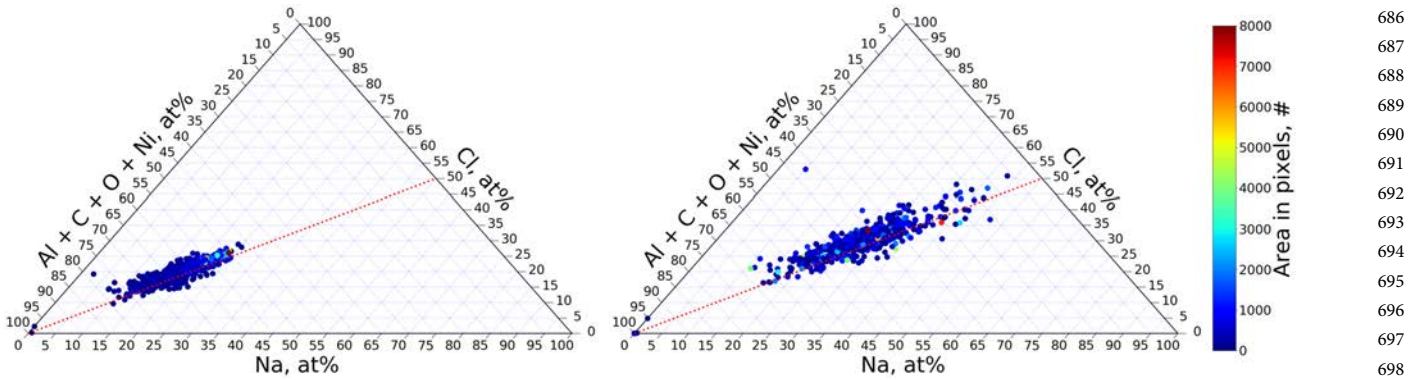


Fig. 10. Ternary plots of at% for Na, Cl, and the sum of all other detected elements, determined from a map acquired at 10 keV with a dwelltime of 512 μ s/pixel. Left: Plot of particle EDS data without substrate subtraction. Right: Plot of particle EDS data with substrate subtraction. Data points are colored according to the particle area in pixels, displayed on the colorbar. The 1:1 line for the Na/Cl at% ratio is plotted as a red dotted line.

aluminosilicate particles from an earlier experiment in the aerosol system. An SE image from this area is shown in Figure 9 (left), along with the results from a feature analysis, where particles were classified based on their elemental composition (middle), as well as an overlay of element maps (right). The overlaying element maps show X-ray counts of various elements, which have been normalized so that the highest count corresponds to a pixel intensity of 255.

Figure 9 shows that much more detail is available from the map compared to the classified image. Overlay of the red Na and the yellow Cl maps yield orange particles, corresponding to NaCl crystals, which, as expected, are fully mixed. A vague blue color covers the entire image, which originates from the Al background signal generated when transmitted or stray electrons hit the sample holder or other stage parts of the microscope. A similar effect would be seen if the element maps for carbon and oxygen had been included, as they are the main components of the Formvar substrate. Cyan-colored particles are also observed, originating from the overlay of green silicon and blue aluminum maps, consistent with the presence of aluminosilicate particles. The map furthermore enables the visualization of the mixing state of particles. Hence, the cyan-colored particle near the center of the classified image, and highlighted in the insert, reveals that an aluminosilicate particle has coagulated with several smaller NaCl particles. In contrast, the feature analysis shows only an integrated particle composition and can therefore not distinguish the four primary particles. The knowledge of particle mixing state can be highly useful for the identification of particle sources in complex atmospheric aerosols. Additionally, maps can be analyzed offline, yielding tables with physical and elemental composition results for each individual particle similar to that obtained by feature analysis. Maps can therefore produce the same results as feature analysis, while providing supplementary information on individual particle mixing state.

Subtraction of Substrate EDS Contribution

Mapping furthermore makes it possible to subtract the substrate/background contribution from individual particle EDS spectra. This is done by determining the mean X-ray count for each element per pixel in the image area recognized as a substrate and subsequently subtracting it from the individual particle X-ray spectra, taking into account the varying particle size. The substrate subtraction will highly influence small particles, with a

Table 2. Overview of the Discussed Advantages and Disadvantages Between Feature Analysis and EDS Mapping as Analysis Strategies for the Characterization of Single Particles.

	Feature Analysis	Mapping
EDS scan setting	Livetime, dwelltime, minimum X-ray count	Dwelltime
Overall analysis time	Depends on setting (shorter)	Constant (longer)
X-ray count small particles	Depends on setting	Low
X-ray count large particles	Depends on setting	High
Drift sensitive	Yes	No
Segmentation	Online	Offline
Revise segmentation	No	Yes
Element segmentation	No	Yes
Particle mixing state	No	Yes
Substrate subtraction	No	Yes

substantial contribution from the substrate, but less so for larger particles. It may be necessary to set negative X-ray counts to zero; in case, the substrate contribution is overestimated. Afterwards, the X-ray counts can be converted to mass% via equation (5) and to at% if needed. Figure 10 shows examples of substrate subtraction made by segmenting an SE image into two phases: a particle phase, containing all pixels with intensities above a set threshold value, and a substrate phase consisting of all pixels with an intensity below a given threshold. The resulting phase-separated image can be seen in the Supplementary Material. The mean substrate pixel X-ray count for all elements were determined from the size and spectrum of the substrate phase, which was subtracted from the individual particle spectra after multiplying with the given particle size in pixels.

Before substrate subtraction, the measured Na + Cl concentration vary from approximately 20 to 50 at% for all NaCl particles, while the remaining concentration is made up of C, O, Ni, or Al, originating from the substrate or inside of the microscope (left

plot in [Figure 10](#)). It is furthermore seen that the Na + Cl content increases with particle size, with the highest concentrations found for the largest particles, as less electrons are transmitted. After substrate subtraction (right plot in [Figure 10](#)), the data points are shifted along the 1:1 line of the Na/Cl ratio, showing that the procedure can distinguish and remove contributions from the substrate and the microscope, while maintaining particle element ratios of Na and Cl. The resulting Na + Cl concentrations range from approximately 30 to 90 at%, hence approaching pure NaCl particles. It is furthermore seen that the size dependency has disappeared, as the substrate contributions for small particles have been significantly reduced. This allows for high Na + Cl concentrations even for small particles with limited X-ray counts. Substrate subtraction can hence be a useful tool when analyzing small particles, where significant contributions from the substrate and the microscope are an issue. However, the method will need additional testing, especially when analyzing particles consisting of elements which are present in the background spectrum. It may also be necessary to introduce size weights, which corrects for the decreasing background contribution with increasing particle sizes.

The discussed advantages and disadvantages between using feature analysis and mapping are summarized in [Table 2](#).

Conclusion

The SEM/EDS analysis of electron transparent beam-sensitive NaCl particles was performed with two types of EDS detectors for comparison, namely the XFlash 6|30, 30 mm² SDD, representing traditional SDD detectors, and the newly developed annular FlatQuad 4 × 15 mm² SDD detector. In this study, the annular detector was found to have a superior count rate, allowing a significant reduction in EDS acquisition time, while ensuring a counting statistics uncertainty below or close to 2%, even for 1 s particle lifetimes. For feature analysis, an EDS livetime of 1 s was found optimal for minimizing beam damage of NaCl particles, as it resulted in Na/Cl ratios close to 1 for all acceleration voltages. Longer lifetimes resulted in the enrichment of Na relative to Cl, indicating beam damage consistent with mechanisms reported in the literature. Here, it was also seen that beam damage was most severe at 5 keV, while the higher degree of transmitted electrons at 20 keV resulted in less. It is therefore recommended to use 20 keV, when analyzing beam-sensitive samples.

Ratios of Na/Cl were compared when quantifying with Cliff-Lorimer or P/B-ZAF. As expected, the P/B-ZAF model was optimal at larger and bulk sizes, though it overcompensated for matrix effects for smaller particle sizes. This was especially obvious at 20 keV, where the P/B-ZAF model overestimated Na/Cl ratios by a factor of 2–3 for all particle sizes used in this study. The Cliff-Lorimer model was found suited for thin samples, though it overpredicted Na/Cl ratios of particles larger than 300 nm at 5 keV. This shows that the transition from transparent to bulk sizes depends on acceleration voltage. The ratio between particle size and electron interaction depth was therefore tested to determine if it could be used as a weight to interpolate results from the two quantification models. The interpolation provided consistent results close to 1 for all particle sizes at all acceleration voltages used in this study. Additional research is needed to confirm its use for larger particle sizes and for particles other than NaCl and potentially those with more complex shapes.

Finally, a comparison was made between EDS mapping and feature analysis, as mapping was found to be a viable option due to the

increased count rates obtainable with the annular detector. The advantages and disadvantages of the two methods are summarized in [Table 2](#), where especially offline and additional segmentation options as well as the higher degree of detail are noteworthy advantages for mapping. Overall, it was shown that the recent advances in EDS detectors allow for detailed sample information on a very short timescale, which enables accurate analysis of nanoparticles and beam-sensitive samples, and makes SEM/EDS analysis more applicable in a broad range of scientific fields.

Supplementary material. To view supplementary material for this article, please visit <https://doi.org/10.1017/S1431927620001464>.

Acknowledgements. The authors acknowledge the Danish Centre for NanoSafety II at the National Research Centre for the Working Environment and the National Centre for Nano Fabrication and Characterization, Technical University of Denmark (DTU) for supporting this PhD study. The authors also acknowledge Bruker Nano, and especially Daniel Goran, for assisting with detector parameters and descriptions, as well as feedback on the final manuscript.

References

- Allen HC, Mecartney ML & Hemminger JC (1998). Minimizing transmission electron microscopy beam damage during the study of surface reactions on sodium chloride. *Microsc Microanal* **4**(1), 23–33.
- Arepalli S, Nikolaev P, Gorelik O, Hadjiev VG, Holmes W, Files B & Yowell L (2004). Protocol for the characterization of single-wall carbon nanotube material quality. *Carbon* **42**(8–9), 1783–1791.
- Armstrong JT & Busseck PR (1975). Quantitative chemical analysis of individual microparticles using the electron microprobe: Theoretical. *Anal Chem* **47**(13), 2178–2192.
- Brodusch N, Demers H & Gauvin R (2018). X-ray imaging with a silicon drift detector energy dispersive spectrometer. In *SpringerBriefs in Applied Sciences and Technology*, pp. 67–84. doi: 10.1007/978-981-10-4433-5_7.
- Brostrøm A, Kling KI, Koponen IK, Hougaard KS, Kandler K & Mølhave K (2019). Improving the foundation for particulate matter risk assessment by individual nanoparticle statistics from electron microscopy analysis. *Sci Rep* **9**(1), 8093.
- Cazaux J (1995). Correlations between ionization radiation damage and charging effects in transmission electron microscopy. *Ultramicroscopy* **60**(3), 411–425.
- Cliff G & Lorimer GW (1975). The quantitative analysis of thin specimens. *J Microsc* **103**(2), 203–207.
- Demers H, Poirier-Demers N, Couture AR, Joly D, Guilmain M, de Jonge N & Drouin D (2011). Three-dimensional electron microscopy simulation with the CASINO Monte Carlo software. *Scanning* **33**(3), 135–146.
- Duncumb P & Reed SJB (1968). The calculation of stopping power and back-scatter effects in electron probe microanalysis. *Quant Electron Probe Microanal* (298), 133–154.
- Egerton RF, Li P & Malac M (2004). Radiation damage in the TEM and SEM. *Micron* **35**(6), 399–409.
- Fletcher RA, Ritchie NWM, Anderson IM & Small JA (2011). Microscopy and microanalysis of individual collected particles. In *Aerosol Measurement: Principles, Techniques, and Applications*, 3rd ed., Kulkarni P, Baron PA, & Willeke K (eds), pp. 179–232. John Wiley and Sons. doi:10.1002/9781118001684.ch10.
- Friel JJ & Lyman CE (2006). X-ray mapping in electron-beam instruments. *Microsc Microanal* **12**, 2–25.
- Hovington P, Timoshhevskii V, Burgess S, Demers H, Statham P, Gauvin R & Zaghib K (2016). Can we detect Li K X-ray in lithium compounds using energy dispersive spectroscopy? *Scanning* **38**(6), 571–578.
- Kandler K, Schneiders K, Ebert M, Hartmann M, Weinbruch S, Prass M & Pöhler C (2018). Composition and mixing state of atmospheric aerosols determined by electron microscopy: Method development and application to aged Saharan dust deposition in the Caribbean boundary layer. *Atmos Chem Phys* **18**(18), 13429–13455.

- Kandler K, Schütz L, Deutscher C, Ebert M, Hofmann H, Jäckel S, Jaenicke R, Knippertz P, Lieke K, Massling A & Petzold A** (2009). Size distribution, mass concentration, chemical and mineralogical composition and derived optical parameters of the boundary layer aerosol at Tinfou, Morocco, during SAMUM 2006. *Tellus B* **61**(1), 32–50.
- Kling KI, Levin M, Jensen ACØ, Jensen KA & Koponen IK** (2016). Size-resolved characterization of particles and fibers released during abrasion of fiber-reinforced composite in a workplace influenced by ambient background sources. *Aerosol Air Qual Res* **16**(1), 11–24.
- Koh AL, Shachaf CM, Elchuri S, Nolan GP & Sinclair R** (2008). Electron microscopy localization and characterization of functionalized composite organic-inorganic SERS nanoparticles on leukemia cells. *Ultramicroscopy* **109**(1), 111–121.
- Laskin A & Cowin JP** (2001). Automated single-particle SEM/EDX analysis of submicrometer particles down to 0.1 µm. *Anal Chem* **73**(5), 1023–1029.
- Laskin A, Cowin JP & Iedema MJ** (2006). Analysis of individual environmental particles using modern methods of electron microscopy and X-ray microanalysis. *J Electron Spectrosc Relat Phenom* **150**(2–3), 260–274.
- Lee JS, Choi YC, Shin JH, Lee JH, Lee Y, Park SY, Baek JE, Park JD, Ahn K & Yu IJ** (2015). Health surveillance study of workers who manufacture multi-walled carbon nanotubes. *Nanotoxicology* **9**(6), 802–811.
- Lee KM, Cai Z, Griggs JA, Guiatas L, Lee DJ & Okabe T** (2004). SEM/EDS evaluation of porcelain adherence to gold-coated cast titanium. *J Biomed Mater Res B* **68**(2), 165–173.
- Newbury DE & Ritchie NWM** (2013). Is scanning electron microscopy/energy dispersive X-ray spectrometry (SEM/EDS) quantitative? *Scanning* **35**(3), 141–168.
- Newbury DE & Ritchie NWM** (2014). Performing elemental microanalysis with high accuracy and high precision by scanning electron microscopy/silicon drift detector energy-dispersive X-ray spectrometry (SEM/SDD-EDS). *J Mater Sci* **50**(2), 493–518.
- Philibert J** (1963). A method for calculating the absorption correction in electron-probe microanalysis. *X-Ray Opt X-Ray Microanal* 379–392.
- Potts PJ** (1987). *A Handbook of Silicate Rock Analysis*, p. 336.
- Reed SJB** (1965). Characteristic fluorescence corrections in electron-probe microanalysis. *Br J Appl Phys* **16**(7), 913–926.
- Ro CU, Osán J, Szalóki I, De Hoog J, Worobiec A & Van Grieken R** (2003). A Monte Carlo program for quantitative electron-induced X-ray analysis of individual particles. *Anal Chem* **75**(4), 851–859.
- Sathirachinda N, Pettersson R, Wessman S & Pan J** (2010). Study of nobility of chromium nitrides in isothermally aged duplex stainless steels by using SKPFM and SEM/EDS. *Corros Sci* **52**(1), 179–186.
- Stebounova LV, Adamcakova-Dodd A, Kim JS, Park H, T O'Shaughnessy P, Grassian VH & Thorne PS** (2011). Nanosilver induces minimal lung toxicity or inflammation in a subacute murine inhalation model. *Part Fibre Toxicol* **8**. doi:10.1186/1743-8977-8-5
- Teng C, Demers H, Brodusch N, Waters K & Gauvin R** (2018). Use of an annular silicon drift detector (SDD) versus a conventional SDD makes phase mapping a practical solution for rare earth mineral characterization. *Microsc Microanal* **24**(3), 238–248.
- Watanabe M & Williams DB** (2006). The quantitative analysis of thin specimens: A review of progress from the Cliff-Lorimer to the new ζ -factor methods. *J Microsc* **221**(2), 89–109.
- Wendt M** (1978). Advances in energy dispersive X-ray microanalysis. *Krist Technol* **13**(11), 1259–1275.
- Wendt M & Schmidt A** (1978). Improved reproducibility of energy-dispersive X-ray microanalysis by normalization to the background. *Phys Status Solidi A* **46**(1), 179–183.